Finding apparent horizons in dynamic 3D numerical spacetimes

Peter Anninos,[1] Karen Camarda,[1,4,6] Joseph Libson,[1,4] Joan Massó,[1,2,6] Edward Seidel,[1,4,6,7] and Wai-Mo Suen[3,5]

[1]*National Center for Supercomputing Applications, 605 E. Springfield Avenue, Champaign, Illinois 61820*
[2]*Departament de Física, Universitat de les Illes Balears, E-07071 Palma de Mallorca, Spain*
[3]*McDonnell Center for the Space Sciences, Department of Physics, Washington University, St. Louis, Missouri 63130*
[4]*Department of Physics, University of Illinois at Urbana-Champaign, Illinois 61801*
[5]*Physics Department, Chinese University of Hong Kong, Shatin, Hong Kong*
[6]*Max-Planck-Institut für Gravitationsphysik, Schlaatzweg 1, 14473 Potsdam, Germany*
[7]*Department of Astronomy, University of Illinois, Urbana, Illinois 61801*

We have developed a general method for finding apparent horizons in 3D numerical relativity. Instead of solving for the partial differential equation describing the location of the apparent horizons, we expand the closed 2D surfaces in terms of symmetric trace-free tensors and solve for the expansion coefficients using a minimization procedure. Our method is applied to a number of different spacetimes, including numerically constructed spacetimes containing highly distorted axisymmetric black holes in spherical coordinates, and 3D rotating, and colliding black holes in Cartesian coordinates. [S0556-2821(98)01414-3]

I. INTRODUCTION

Black holes are among the most fascinating predictions in the theory of general relativity. The black holes most likely to be observed by future gravitational wave observatories [Laser Interferometric Gravitational Wave Observatory (LIGO) and VIRGO [1]] are those in highly dynamical evolutions, such as two colliding black holes. Moreover, events which are important for observations (i.e., events that occur more frequently and emit stronger radiation) are not expected to have a high degree of symmetry; for example, the inspiraling coalescence is a more probable scenario than the axisymmetric head-on collision of two black holes. The most powerful tool in studying such highly dynamical and intrinsically non-linear events is numerical treatment.

The essential characteristics of a black hole are its horizons, in particular, the apparent horizon (AH) and the event horizon (EH). One needs to determine the location and the structure of the EH's in numerical studies to understand the properties of black holes, and indeed even to assert the existence of the holes. Algorithms for doing this have recently been developed [2,3]. In contrast, the problem of determining the location of the AH in a general numerically constructed 3D spacetime has not yet been solved satisfactorily. The present paper represents a step in this direction.

The apparent horizon is defined to be the outer-most marginally trapped surface [4], a surface for which the divergence of the out-going null normal is zero [cf., Eq. (1) below]. The surface is defined locally in time, in contrast to the EH, which can only be identified after the numerical simulation is complete. The AH, as a characteristic of black holes, can be used *during* the numerical construction of the spacetime. As discussed in a number of publications, apparent horizons are useful not only for studying the dynamics of black hole spacetimes [5], but also for use as an inner boundary in numerical evolutions of black holes [6–8]. The so-called apparent horizon boundary condition (AHBC) is currently being developed by many groups as a promising

method for use in computing the long term evolution of 3D black hole systems. With AHBC one would like to be able to track the AH throughout the numerical evolution. For these reasons, it is important to develop efficient methods for locating apparent horizons in numerically constructed spacetimes.

There are many well developed methods for determining the location of AH's in lower dimensional spacetimes [9–13], e.g., in axisymmetry. The partial differential equation (PDE) defining a marginally trapped surface [Eq. (1) below] reduces to an ordinary differential equation (ODE) in the axisymmetric case, and the symmetry conditions also provide boundary conditions for starting the integration of the ODE. This simplifies tremendously the problem, and enables the construction of efficient methods for finding the AH. However, as these methods rely strongly on the symmetry assumptions, they are not generalizable to 3D; going from 2D to 3D does not amount to simply adding one more spatial dimension. For the general 3D case, there is no symmetry and the AH surface to be determined is a *closed* surface (hence no boundary conditions for starting the integration) described by a non-linear elliptical PDE. At present there are no efficient algorithms for solving such a partial differential problem in general.

We are aware of three independent efforts in determining the AH in the general 3D case. The first method is based on an expansion of the AH surface in terms of spherical harmonics, with the expansion coefficients determined by an integral equation. The equation is then solved iteratively [14,15]. The second method attempts to solve directly the elliptic PDE [16,17]. The third method [18] is based on expanding the closed surface in terms of orthogonal functions, in particular symmetric trace-free (STF) tensors, and using a minimization procedure to determine the expansion coefficients. Variations on this idea were explored by Brill and Lindquist [19] and by Eppley [20]. The essential difference of this method with the first method is in the way the expansion coefficients are determined, and the use of STF tensor

expansions for 3D Cartesian codes. The major advantage of this method is that the numerical solution of the minimization problem is much better understood than the corresponding PDE problem. In Ref. [18], we demonstrated that our method can be efficiently applied to testbeds made up of analytically given data sets representing time-symmetric slices of spacetime. In Ref. [21], the convergence of the symmetric trace-free tensor expansion for similar testbeds is studied in detail. In this paper, we follow up on our earlier work and give a more detailed discussion of this method. We also push the application of it in two directions: (1) Application of the method to arbitrary data sets which are not time-symmetric (non-zero extrinsic curvature), and (2) application of the method to data obtained in actual numerical evolutions of dynamical spacetimes. The spacetimes we studied include Schwarzschild and Kerr black holes, black hole plus Brill wave, and Misner two black hole spacetimes in full 3D. We demonstrate that our method is in principle applicable to general $3+1$ spacetimes. Another method presently under development also uses a series expansion as in the present method, but it evolves the trial surface to the AH in an algorithm that combines elements of the AH finder of [14] and of a curvature flow method [22].

In Sec. II we discuss the formulation of our method, and the numerical algorithm in detail. Section III gives the results of various testbed calculations, with Sec. III A concentrating on initial data sets, and Sec. III B on spacetime evolutions. Section IV concludes with a discussion of where we stand in the construction of a general method for finding apparent horizons in 3D numerical relativity.

II. FORMULATION OF THE AH FINDER

A. Basic equations

Defining s^μ to be the outward-pointing spacelike unit normal of a two-sphere $\mathcal{S}$ embedded in a constant time slice Σ with unit normal n^μ, we can construct the outgoing null normal to any point on $\mathcal{S}$ as $k^\mu = n^\mu + s^\mu$. The surface $\mathcal{S}$ is called a *marginally trapped surface* (MTS) if the divergence of the outgoing null vectors vanishes $\nabla_\mu k^\mu = 0$, or equivalently [23]

$$\Theta = D_i s^i + K_{ij} s^i s^j - K = 0, \tag{1}$$

where Θ is the expansion of the outgoing rays, D_i the covariant derivative with respect to the 3-metric γ_{ij}, K_{ij} the extrinsic curvature of Σ, and K the trace of K_{ij}. The AH is defined as the outer-most trapped surface.

First suppose we are searching for the AH of a single black hole in spherical coordinates. As the AH is topologically a 2-sphere [24], its position can be represented as

$$F(\theta,\phi,r) = r^2 - f(\theta,\phi) = 0. \tag{2}$$

The unit normal s^i

$$s^i = \gamma^{ij} \partial_j F (\gamma^{kl} \partial_k F \partial_l F)^{-1/2}, \tag{3}$$

can then be expressed in terms of the function $f(\theta,\phi)$. Substituting Eqs. (2) and (3) into Eq. (1), one gets an elliptic

equation for $f(\theta,\phi)$. Instead of solving this elliptic equation directly, we proceed by expanding f in terms of the usual spherical harmonics Y^{lm}:

$$f(\theta,\phi) = \sum_{l=0}^{L} \sum_{m=-l}^{l} F^{lm} Y^{lm}(\theta,\phi). \tag{4}$$

Equation (1) then gives Θ in terms of the expansion coefficients F^{lm}. The AH can be determined by finding the set of coefficients F^{lm} which make $\Theta = 0$.

For 3D codes in Cartesian coordinates, instead of the spherical harmonic expansion (4), we choose to expand the trial surfaces in terms of symmetric trace-free (STF) tensors:

$$F(x,y,z) = \sum_{i=1}^{3} (x^i - x_0^i)^2 - \sum_{l=0}^{L} \mathcal{F}_{K_l} N_{K_l} = 0, \tag{5}$$

where x^i are Cartesian coordinates and x_0^i the Cartesian points interior to the $F=0$ surface representing the horizon center. In expanding the function f in Eq. (5), we have adopted the notation from Ref. [25]. The STF tensors $\mathcal{F}_{K_l}$ are coordinate independent coefficients, the subscript K_l is abbreviated notation for the vector product $N_{K_l} \equiv n_{k_1} n_{k_2} \dots n_{k_l}$, and the n_i are unit directional vectors

$$n_i = \frac{x^i - x_0^i}{\sqrt{\sum_{j=1}^3 (x^j - x_0^j)^2}}. \tag{6}$$

To determine the set of $\mathcal{F}_{K_l}$ which makes Eq. (5) the AH, we use a minimization procedure. In general, the AH surface is the outer-most surface represented by the set of $\mathcal{F}_{K_l}$ and x_0^i which satisfy

$$\sum_\sigma W_\sigma \Theta_\sigma^2 (\mathcal{F}_{K_l}, x_0^i) = 0. \tag{7}$$

Θ^2 is semi-positive definite. W_σ is a positive definite weighting function which can be chosen to improve the accuracy of the minimization procedure depending on the construction of the trial surface. In this paper we do not investigate the use of this parameter and set $W_\sigma = 1$. With this we have converted the elliptic condition (1) to a standard minimization problem. There are efficient minimization algorithms to search the space of $(\mathcal{F}_{K_l}, x_0^i)$ coefficients for the surface closest to the apparent horizon among all test surfaces so parametrized. The strength of our method lies in that the minimization problem is much better understood than the numerical solution of the corresponding differential equation (1).

An obvious potential difficulty of this method is that there is no guarantee that the summation (5) converges, or converges rapidly. For black holes not in highly dynamical situations, we do expect the AH surface to be smooth and one needs only the first few lower rank tensors to find the surface accurately (as demonstrated in Sec. III). This is usually the case through most of the simulations, and our method will be more efficient at these times. However, we also expect that, for the cases we would like to simulate, there are often pe-

riods of time when the black hole (or holes) goes through highly dynamical evolutions, e.g., around the moment of the coalescence of two black holes. In such cases, one needs higher order STF expansions. Although STF tensor expressions are available in the literature, we find it convenient to include in our code a routine for the automatic generation of STF tensors to an arbitrarily high order. The procedure takes advantage of the fact that we can associate the n_i with essentially $x-x_0$, $y-y_0$ or $z-z_0$ in three dimensions. We can therefore construct all symmetric and independent permutations of

$$N_{K_l} \equiv A_l(x-x_0)^\alpha(y-y_0)^\beta(z-z_0)^\gamma, \qquad (8)$$

subject to the constraint $\alpha+\beta+\gamma=l$, where l is the rank of the corresponding symmetric tensor, or equivalently the order of the multipole expansion, and A_l is the normalization factor making the right-hand side (RHS) dimensionless. There are $(l+1)(l+2)/2$ such independent combinations. The combinations constructed in this fashion can be supplemented with the $l(l-1)/2$ independent conditions imposed on the symmetric permutations to make the rank l tensor trace-free by contracting on any two indices. The function f can be expanded as

$$f(x,y,z) = \sum_{l=0}^{L} \sum_{k}^{\alpha+\beta+\gamma=l} C_k \langle (x-x_0)^{\alpha_k}$$
$$\times (y-y_0)^{\beta_k}(z-z_0)^{\gamma_k} \rangle, \qquad (9)$$

where C_k are coordinate independent coefficients, and $\langle \rangle$ denotes STF combinations [25]. Partial derivatives $\partial_i F$ and $\partial_i \partial_j F$ needed to evaluate Θ on the trial surfaces are then easily computed from Eqs. (2) and (9). The simplicity of the form (9) also allows one to easily construct the multipole expansion to take advantage of any symmetries present in the problem. For instance, our current implementation, by setting a flag, can invoke either the even or odd multipoles independently of the other, enforce axisymmetry, fix the surface centers x_0^i, or allow the most general parametric expansion.

B. Numerical algorithms

The numerical problem is to find a set of parameters (C_k, x_0^i) that minimizes the LHS of Eq. (7). Minimization techniques (such as conjugate gradient or quasi-Newton methods) that evaluate both the function and all its various partial derivatives are often preferred, as a means to increase the convergence rate, to those that do not require derivative information. However, because of the complexity of Eq. (1), in this first generation 3D AH finder we have chosen to implement a multi-dimensional method that does not require knowledge of derivatives, namely a direction set or Powell's method [26]. The method is based on successive line minimizations, whereby the function $\Sigma\Theta^2$ is successively minimized along different vector directions using the one-dimensional Brent's method with parabolic interpolation. We find Powell's method to be generally robust, with a good convergence rate and computational speed, for surface functions parameterized by fewer than about fifteen or so parameters (see Sec. III). Although solutions can still be found for parametrizations of higher order, the computational cost becomes overly excessive, especially when compared to the evolution cycle time.

A two-grid system is utilized to evaluate the expansion function Θ. The first grid (which we refer to as grid A) is the Cartesian-based computational grid on which the Einstein evolution and constraint equations are solved, and the metric and extrinsic curvature components are defined. A second grid B is used to evaluate the surface function $F(\theta,\phi,r)$. This second grid need not be structured in the same way as the first.

Assuming a guess position for the horizon center $x_0^i=(x_0,y_0,z_0)$ on the structured Cartesian grid A, and some prescription for distributing points throughout this mesh to construct nodes for the second grid B, we can evaluate the expansion Θ on the nodes of grid B once $f(\theta,\phi)$ is determined. Here we choose to distribute the nodes uniformly over a sphere, centered on x_0^i: the nodes are evenly spaced in both the polar and azimuthal angles to cover the full sphere $0 \leq \theta \leq \pi$ and $0 \leq \phi \leq 2\pi$ (or a single octant for the axi- and equatorial symmetric spacetimes). However, this procedure can easily be generalized to, for example, weight the node distribution according to the coordinate surface curvature, as might be desirable for highly distorted horizons. Along the radial direction, the nodes of grid B are placed uniformly with an inter-node spacing δr typically equal to the cell resolution of grid A on which the Einstein equations are solved. We have also implemented a procedure to constrain the range of radii over which the solver searches for the AH, as might be desirable in cases where multiple trapped surfaces exist in the data set. In these cases, the radial grid spacing is set by $\delta r=(r_{max}-r_{min})/N_r$, where N_r is the number of radial nodes, and r_{min} and r_{max} are the lower and upper bounds of allowable radii. Representing the number of nodes on grid B as $N_\theta \times N_\phi \times N_r$, we set $N_\theta=N_\phi=5$ along the angular directions in a single octant, and $N_r=N$ along the radial direction, where N is the minimum number of cells among the three orthogonal axes in grid A.

Once the spherical grid B is constructed and centered on x_0^i, the function F in Eq. (2) is evaluated on the nodes of grid B for a fixed set of coefficients (C_k, x_0^i) that the Powell routines compute. Along each radial line, a search is made for $F=0$, by scanning from large to small radii, until the condition $F(\theta,\phi,r) \times F(\theta,\phi,r+\delta r)<0$ is met, and then linearly interpolating between adjacent neighbors to find the approximate Cartesian coordinates of the surface corresponding to $F=0$. The extrinsic curvature and the metric functions and their derivatives are then evaluated at these positions by interpolating (either linearly or quadratically) from the computational grid A on which they are defined and used in Eq. (1) to evaluate Θ^2 on the surface. The process of constructing a spherical grid B centered on x_0^i, evaluating F on grid B, searching for the surface coordinates for which $F=0$, interpolating the geometric data to the surface, and evaluating the expansion (1) on the surface is repeated through

Powell's procedure until a minimum of $\Sigma\Theta^2$ in the parameter space (C_k, x_0^i) is realized.

To reduce the computational time spent in finding apparent horizons and to make the finder usable in real time evolutions of black hole spacetimes, it is important to implement the solver in a parallel fashion. Fortunately, the calculations performed at each node on the trial 2D surfaces are independent of the other node calculations. A natural parallel implementation, which we have adopted, thus distributes the different surface calculations to different computational processors, achieving a speedup of $N_\theta \times N_\phi$ compared to a purely scalar code. In addition, a large percentage of the cpu time is spent interpolating the field variables from grid A onto the 2D surface. To speedup this bottleneck procedure, we have written and implemented generalized algorithms designed to interpolate (both linearly and quadratically) 3D data onto different nodes within a 2D surface in parallel. The computationally intensive elements of the horizon finder have been optimized for both the Cray C90 and the massively parallel Thinking Machines CM5 computers.

III. CODE TESTS

In order to test the basic solver described above, we have developed both 2D and 3D AH finders based on this minimization method.

For the 2D finder, the AH determined can be directly compared to those obtained with the standard integration method. As testbeds, we used data obtained from a code developed by Bernstein *et al.* [27]. This code evolves a black hole distorted by an axisymmetric distribution of gravitational waves (Brill waves) [28]. The black holes can be highly distorted by the incoming waves, leading to AH's with extremely prolate or oblate geometric shapes. In some cases the ratio of polar to equatorial circumference can exceed 10^2. When these systems are evolved, the horizons undergo dynamic oscillations, eventually settling down to a Schwarzschild black hole at late times [5]. For such dynamic spacetimes, we compared the results obtained with our new AH finder algorithm with those from the AH finder constructed using the standard ODE method [13,5]. For test surfaces with 16 coefficients, and using spherical harmonics Y_{lm} as basis functions, we find that both methods produce the same results to within the given accuracy of the PDE solvers.

As this paper is on a 3D implementation of these ideas for finding AH's, in the following we concentrate on results for the 3D case only. We have written a Fortran routine that implements the above method for a general 3D spacetime in Cartesian coordinates, and tested it on various spacetimes of interest. We discuss results from this code applied to various initial data sets containing one or more black holes (Sec. III A), and to evolutions of some of these black hole spacetimes carried out with our 3D ''G'' code [29] (Sec. III B). For all the 3D tests, we use the symmetric trace-free (STF) tensors as basis functions defined on a unit sphere.

A. Finding horizons in initial data sets

1. Schwarzschild black hole

The simplest, most basic, test for any apparent horizon finder is the static Schwarzschild initial data. The 3-metric can be written in Cartesian coordinates as
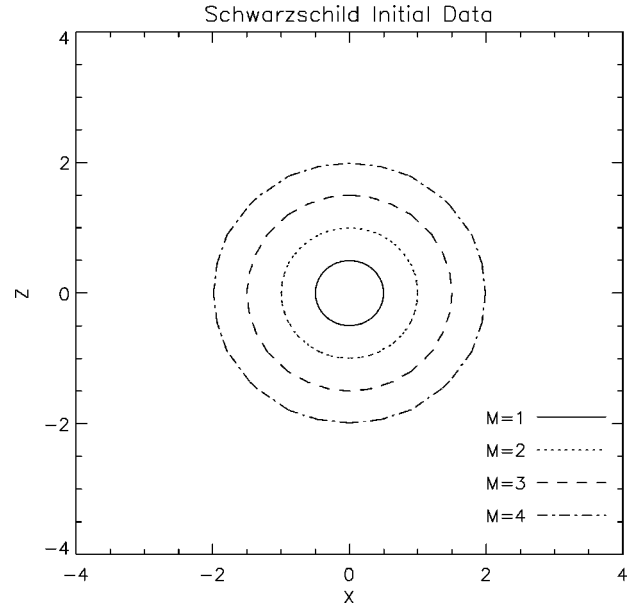

FIG. 1. The coordinate location of the apparent horizon in the x-z plane for Schwarzschild initial data with various masses. The computed surfaces are indistinguishable from the analytic solutions, with deviations of order 0.04%.

$$dl^2 = \left(1 + \frac{M}{2r}\right)^4 (dx^2 + dy^2 + dz^2), \qquad (10)$$

where M is the mass of the black hole. The apparent horizon in this case is spherically symmetric and located at $r = M/2$. Although only the $L=0$ term should contribute to the surface that defines the apparent horizon, we tested the solver with a more general multipole expansion with the $m \neq 0$ terms up to and including $L=6$, a total of 28 coefficients.

The computed surface is plotted in Fig. 1 for four separate cases with various black hole masses. The grid resolution used in each case was $\Delta x = \Delta y = \Delta z = 0.075M$, using 25^3 cells. As expected, the surface is mostly defined by the $l=0$ contribution: The other higher order terms are small in comparison, roughly a factor of 10^{-8} smaller. We find typical errors in the horizon radius of order 0.04%, and the numerical surfaces are indistinguishable from the analytic solution in Fig. 1. In each of the cases shown here, the finder converged to the correct surface in approximately 30 iterations. However, the number of iterations decreases significantly if fewer parameters are varied. For example, only 3 iterations are needed to converge if only the monopole term is varied, reducing the computational time by a factor of 60. On average, the CPU time scales approximately as N_p, where N_p is the number of parameters. Hence, the method becomes rather cumbersome for highly distorted horizons which can only be described with a high order multipole expansion. We discuss this important issue further in the following more elaborate tests.

2. Misner data

The Misner initial data set represents two equal mass black holes initially at rest, and is defined by the 3-metric
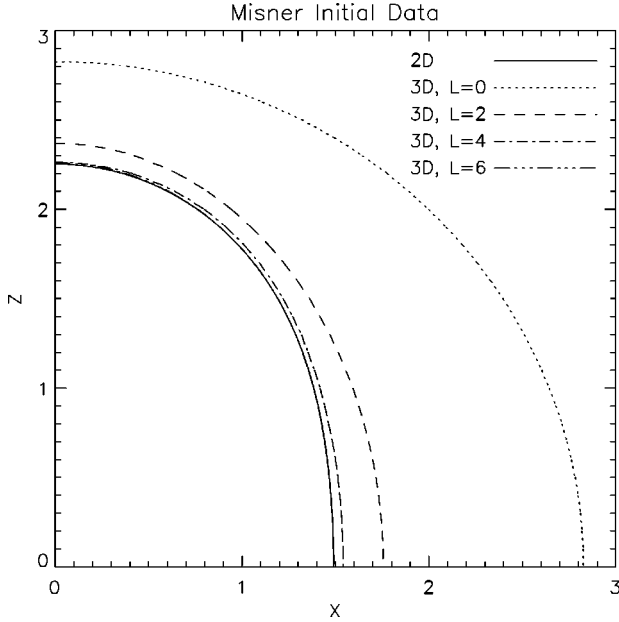
FIG. 2. The coordinate location of the apparent horizon for the $\mu = 1.2$ Misner initial data. The solid line is the apparent horizon computed from our 2D code. The various broken lines are the surfaces obtained from the different multipole order expansions. The surface obtained from the $L=6$ expansion is indistinguishable from the 2D result in this plot. We note that terms up to $L=6$ must be included to find the AH accurately.

$$dl^2 = \psi^4(dx^2 + dy^2 + dz^2), \qquad (11)$$

where

$$\psi = 1 + \sum_{n=1}^{\infty} \frac{1}{\sinh(n\mu)} \left(\frac{1}{{}^+r_n} + \frac{1}{{}^-r_n} \right), \qquad (12)$$

and

$$^\pm r_n = \sqrt{x^2 + y^2 + [z \pm \coth(n\mu)]^2}. \qquad (13)$$

The parameter μ specifies the proper separation between the two holes and the total ADM mass of the spacetime. Apparent horizons in these data sets may consist of either a single surface surrounding both black holes if they are sufficiently close to one another ($\mu < 1.36$) [30], or two separate horizons located at the throats of the holes.

In the cases where the two holes form a single encompassing horizon, the surface can be distorted significantly. To find the distorted horizons accurately, then, we need to keep higher order multipole terms, but *a priori* it is not clear how many terms will be required. In Fig. 2, we show the results of systematically increasing the number of axisymmetric expansion terms for the case $\mu = 1.2$. In each calculation we use a 64^3 grid with $\Delta x = 0.1$ and run the code on the 128 node partition of the CM5. We also show the result obtained with our 2D, axisymmetric code described in Ref. [31], which implements an independent ODE integration method [5]. It is obvious that a high order expansion, up to $L=6$, is required to accurately describe this surface which has a major to minor axis ratio of 1.5. We expect that even higher

TABLE I. The effect of the (axisymmetric) multipole order L on finding the correct horizon surface is demonstrated here for the two black hole Misner data with $\mu = 1.2$. The number of iterations and CPU time required by the solver is tabulated along with the expansion summed over all points on the surface. The timings were performed on the 128-node partition of the CM5, using a 3D grid of size 64^3 and a 5×5 mesh to cover the 2D horizon surface in a single quadrant.

L	Iterations	CPU time	$\Sigma \Theta^2$
0	2	1.2 min	8.3×10^{-2}
2	5	2.2 min	8.0×10^{-3}
4	9	4.6 min	7.9×10^{-4}
6	16	12 min	1.0×10^{-4}

multipole expansions would be required for more distorted surfaces. In Table I, we show the number of iterations, CPU time and $\Sigma \Theta^2$ as a measure of convergence for each of the expansion orders. We note that timings reported here and throughout this paper refer to the Thinking Machines CM5.

For $\mu > 1.36$, there are two separate and spherical trapped surfaces on the initial slice, centered off the origin at $z = \pm \coth \mu$. In the cases we have tested ($\mu = 2.0$ and 2.2), the solver is able to locate both the center and radius of the offset horizons to an accuracy of better than 0.06% using general expansions to any order, $L=0$ to $L=6$. We note that the iteration count (and hence CPU time) can increase by factors of between 2 to 10, depending on the total number of parameters, as compared to the cases in which the throat center coordinates are not allowed to vary.

3. Black hole plus Brill wave

The Misner initial data family just discussed provides examples of both single perturbed horizons and two separate but spherical surfaces with offset centers for testing. However, black hole horizons in highly dynamic spacetimes can be extremely distorted geometrically, and the horizon finder must be able to locate these as well. The black hole plus Brill wave initial data set is yet another solution that has been studied extensively in axisymmetry, and thus provides a useful testbed for highly distorted holes in three dimensions. This data describes the superposition of a black hole and a ''doughnut'' shaped Brill wave surrounding the hole. In spherical coordinates, the 3-metric takes the form

$$dl^2 = \psi^4(e^{2q}(dr^2 + r^2 d\theta^2) + r^2 \sin^2\theta d\phi^2), \qquad (14)$$

where q and ψ are functions of r and θ only. The function q is specified analytically as free data, and the Hamiltonian constraint is solved for the conformal factor ψ. The initial extrinsic curvature vanishes due to time symmetry.

This data set has been studied with 2D, axisymmetric codes [13,28] using a logarithmic radial coordinate $\eta = \ln(2r/m_0)$, where m_0 is a scale parameter. In this coordinate system (η, θ, ϕ), the form of the q-function is written as
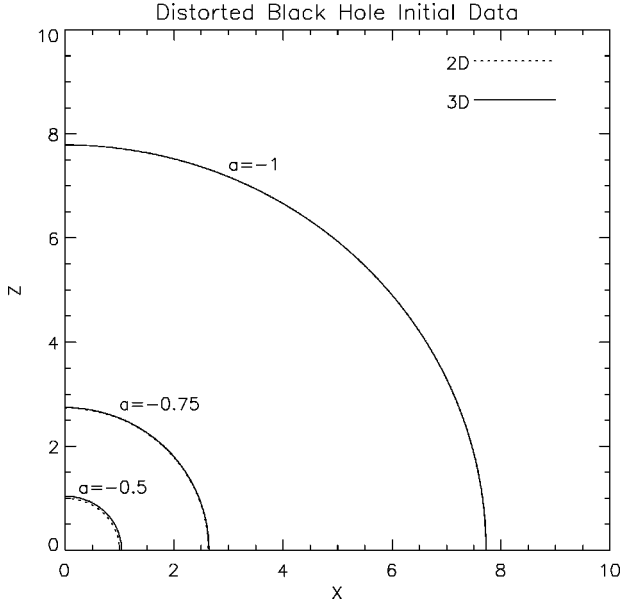
$$q = a \sin^n \theta g(\eta), \qquad (15)$$

FIG. 3. The coordinate location of the apparent horizon for 2D and 3D Brill wave plus black hole initial data with various values of the Brill wave amplitude. In all runs, the Brill wave is centered at $\eta_0 = 0$ and has a width of $\sigma = 1$. Note that there is good agreement even though the initial data is not analytic and actually contains highly geometrically distorted black hole horizons.

where we set $n = 2$, and

$$g(\eta) = \exp\left[-\left(\frac{\eta + \eta_0}{\sigma}\right)^2\right] + \exp\left[-\left(\frac{\eta - \eta_0}{\sigma}\right)^2\right]. \quad (16)$$

We solve the Hamiltonian constraint for the conformal factor in our 2D code and then interpolate these solutions onto a 64^3 Cartesian grid with $\Delta x = 0.15$ to generate 3D data sets. The 3D horizon finder is tested against an independent solver developed for 2D calculations [13].

In Fig. 3 we show the coordinate location of the apparent horizon for various parameters of the q-function. The sequence shown corresponds to different values of the Brill wave amplitude a, for fixed ''shape'' parameters having the values $(\eta_0, \sigma, n) = (0,1,2)$. Results from both the 2D and 3D calculations are shown. In the 3D case, we allowed searches up through $L = 4$, but for this case we include only the axisymmetric terms. In all cases shown, the finder was able to locate the correct surface to within a third of a grid zone in just 6 iterations.

Figure 4 is a resolution convergence study of the case $a = -0.75$ in which the cell size is varied from $\Delta x = 0.6$, 0.3 and 0.15 with 16^3, 32^3 and 64^3 grids respectively. The solver clearly converges to the correct surface quadratically with cell size.

For negative values of the Brill wave amplitude parameter a, the horizon is found off the throat, but for positive values below certain limits (depending on the shape parameters) the horizon is located on the throat at $r = m_0/2$. We are also able to locate the AH at the same level of accuracy for these cases.
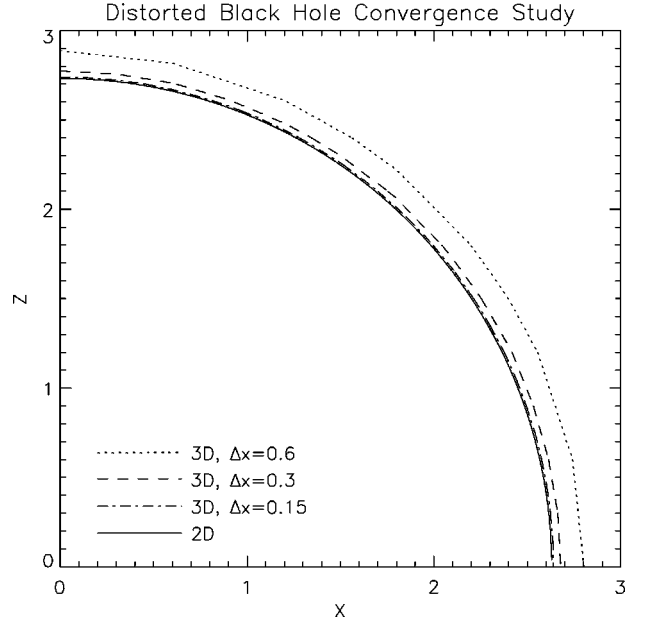

FIG. 4. A resolution study of the Brill wave plus black hole spacetime for the case $(a, \eta_0, \sigma) = (-0.75, 0, 1)$. The surface converges quadratically with grid spacing to the correct location, as represented by an independent 2D calculation shown by the solid line.

Although the surfaces shown in Fig. 3 appear to be almost spherical in coordinate space, the presence of strong gravitational waves can severely distort the horizons geometrically, much more so than the Misner data solutions described above. In Fig. 5 we show the (axisymmetric) geometric embedding of the two cases $a = \pm 1$, using the method described in Ref. [5]. For all negative values of the amplitude parameter, the horizon is oblate. The $a = +1$ case is highly distorted geometrically into a prolate shape, with a ratio of polar to equatorial circumference of $C_p / C_e = 4.28$.

4. Kerr black hole

The calculations presented so far have tested the ability of the solver to find single or multiple horizons of spherical and highly distorted black holes in 3D Cartesian coordinates. However, the data in all these cases are time symmetric. The Kerr initial data set describing a rotating black hole has non-trivial extrinsic curvature, and thus provides another important testbed with a known analytic solution. The 3-metric for this spacetime in Boyer-Lindquist coordinates is given by

$$dl^2 = \frac{\rho^2}{\Delta}dr^2 + \rho^2 d\theta^2 + \frac{((r^2 + a^2)^2 - \Delta a^2 \sin^2\theta)\sin^2\theta}{\rho^2}d\phi^2, \quad (17)$$

where

$$\rho^2 = r^2 + a^2\cos^2\theta, \quad (18)$$

$$\Delta = r^2 - 2Mr + a^2. \quad (19)$$

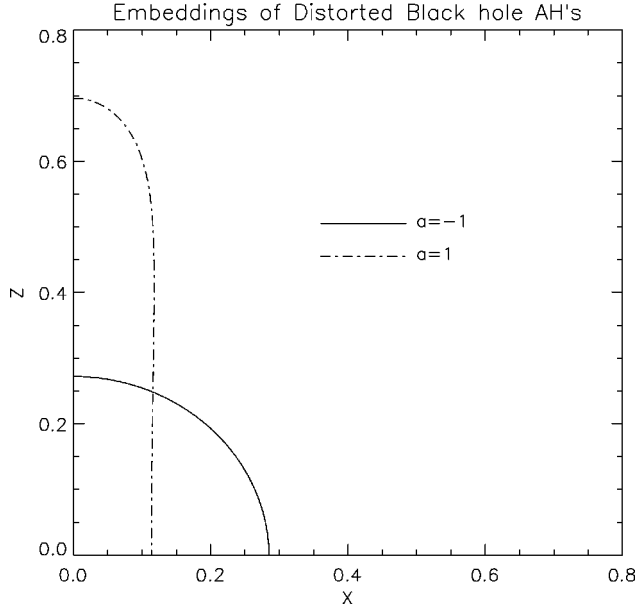In these coordinates, the non-vanishing components of the extrinsic curvature are

FIG. 5. The geometric embedding diagrams of the apparent horizons for the Brill wave plus black hole initial data with wave amplitudes $a=\pm 1$. The $a=-1$ horizon is quite oblate, and deviates from sphericity even in its coordinate location. For the $a=1$ case, the horizon is actually located on the throat, which is a coordinate sphere. However, the metric functions are highly nonspherical, leading to this very prolate geometry of the horizon surface.

$$\hat{K}_{r\phi}=aM[2r^2(r^2+a^2)+\rho^2(r^2-a^2)]\sin^2\theta/(r\rho^4),$$

(20)

$$\hat{K}_{\theta\phi}=-2a^3Mr\sqrt{\Delta}\cos\theta\sin^3\theta\rho^{-4},$$

(21)

where $\hat{K}_{ij}=\psi_0^2 K_{ij}$, and

$$\psi_0^4=\frac{(r^2+a^2)^2-\Delta a^2\sin^2\theta}{\rho^2}.$$

(22)

To construct this data in 3D, we first transform to an isotropic radial coordinate through the transformation

$$r=\bar{r}\left(1+\frac{M+a}{2\bar{r}}\right)\left(1+\frac{M-a}{2\bar{r}}\right),$$

(23)

as described in [32]. In this coordinate system, the coordinate singularities at $r=M\pm\sqrt{M^2-a^2}$ disappear. We then convert

the metric and extrinsic curvature from isotropic coordinates to Cartesian coordinates. The apparent horizon for the Kerr data is a coordinate sphere, located at

$$\bar{r}=\frac{\sqrt{M^2-a^2}}{2}.$$

(24)

In Table II we show results from runs with various values of the rotation parameter a/M and expansion order L. These runs were all done with general expansions, without restricting to axisymmetry. For the tests performed here, Δx, Δy and Δz were chosen to be approximately one tenth of the analytic AH radius, and the number of cells (32^3) was kept the same in all cases. Only the $l=0$ contributions are shown. As expected, the contributions from higher-l terms are small, ranging from 10^{-9} for $a/M=0$ to 3×10^{-2} for $a/M=0.9$. The reason that these terms, in the highly rotating cases, are not as small as in the Schwarzschild case is because the metric is not conformally flat, so the interpolations within the finder are not as accurate. Although we do not display embeddings of these horizons, we note that rotating black hole horizons can be extremely oblate, and for rotation parameters $a/M>0.866$ a global embedding into Euclidean space is not possible. The horizon finder has no difficulty in locating these surfaces to within a grid zone, although we note, again, the high computational cost for large order multipole expansions as indicated by the $a/M=0.3$ sequence of calculations.

5. Transformed Schwarzschild black hole

The above test cases, although treated in full 3D, have all been axisymmetric. In this section we test our finder on data which does not have any particular symmetry, and for which we can derive the correct solution in order to gauge the accuracy of the solver. To this end, we chose to find the apparent horizon on a Schwarzschild initial slice using a coordinate system in which the horizon surface does not appear to be axisymmetric. The coordinate transformation we use is

$$\bar{r}=rf(\theta,\phi)=r\left(1+\frac{1}{4}\sin^2\theta(\cos^2\phi-\sin^2\phi)\right)^{-1/2}$$

(25)

where r is the radial isotropic coordinate of Eq. (10). This $f(\theta,\phi)$ has surface modes of $L=2$. The apparent horizon location is then defined by $\bar{r}=(M/2)f(\theta,\phi)$.

TABLE II. Performance measures of the horizon solver applied to the Kerr black hole data with various spin parameters a/M. Here L is the maximum multipole order, Δx is the 3D grid spacing, r_a is the analytical position of the horizon, r_n is the horizon location found by the solver, and $\Delta r/\Delta x$ is the difference between the analytic and numerical locations normalized to the grid spacing. We also show the number of iterations and CPU time required by the solver running on a 32-node partition of the CM5, using a grid with 32^3 cells and a 5×5 mesh for the surface.

a/M	L	Δx	r_a	r_n	$\Delta r/\Delta x$	Iterations	CPU
0	4	0.1	1.0	1.0002	0.003	30	2.4 h
0.3	4	0.1	0.954	1.0095	0.556	37	1.0 h
0.3	2	0.1	0.954	0.9562	0.022	9	6.7 min
0.3	0	0.1	0.954	0.9542	0.002	2	0.5 min
0.9	4	0.039	0.436	0.4748	0.997	27	0.5 h

The solver was allowed to search coefficients with terms up to $L=2$ and $L=4$. In all cases for the $L=2$ tests, the finder successfully found the horizon to high accuracy. Each non-zero coefficient was accurate to better than a tenth of one percent, and the largest value found for a coefficient that was supposed to be zero was less than 2% of the smallest non-zero component. We note that better accuracy can be achieved if one uses full knowledge of the analytic form of the metric. When the finder was generalized to allow searches with coefficients up to $L=4$, the horizon was again successfully found and to comparable accuracy. However with the large number of search parameters, some care was necessary in choosing the initial search direction of the Powell routine in order to avoid getting trapped at local minima in Θ^2 generated in the discretized representation of the spacetime. When the resolution of spacetime grid is increased, such local minima will disappear/change in location, in sharp contrast to the actual $\Theta^2=0$ point (the actual location of the AH, which converges to a fixed location with increased resolution.) In Fig. 6, we show the apparent horizon found and the analytic solution in one quadrant of each of the coordinate planes. The numerical results shown in this figure were obtained with a run in which coefficients up to $L=4$ were allowed to vary.

B. Evolved 3D data sets

The tests described thus far have shown that the horizon finder can locate horizons in a variety of distorted black hole spacetimes, but these have all been initial data sets with a somewhat restricted 3-metric and extrinsic curvature, and with a large part of the data prescribed analytically. In general 3D black hole evolutions, all metric and curvature components will be present, and the data will be contaminated with numerical inaccuracies generated during the course of evolution. The horizon finder must work under these conditions for it to be a useful tool in the numerical construction of spacetimes. In this section, we discuss results derived from the implementation of the horizon solver into our 3D ''G'' code [29] that solves the Einstein evolution equations in Cartesian coordinates.

1. Schwarzschild

The tests discussed here were carried out using multipole expansions up to and including the $L=4$ terms. However, in order to save computational time, we restricted the search to axisymmetric surfaces. We have verified that a more general expansion does not change the results significantly.

The results for a 3D Schwarzschild spacetime, evolved with both geodesic and maximal slicings with zero shift, are shown in Figs. 7 and 8 respectively. A $64^3(130^3)$ grid with $\Delta x=0.15(0.2)$ was used for the geodesic (maximal) case with $\Delta t=0.25\Delta x$. Only the $l=0$ contribution to the surface is plotted. The other parameters remain small $(<10^{-3})$ during the entire evolutions, as expected. In both cases, the surface locations are compared against the corresponding results from 1D calculations. The two results agree to a small fraction of a grid zone throughout the evolution. The late time deviation in the maximal run is attributed to errors in the 3D
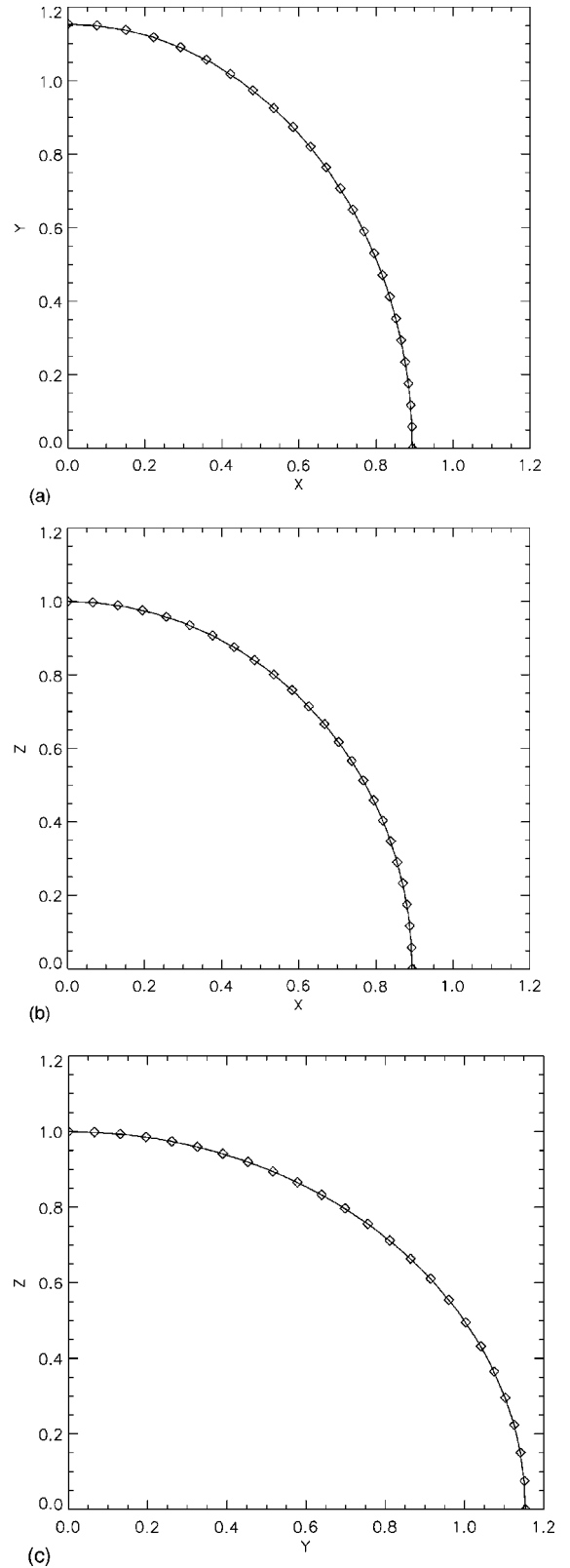

FIG. 6. Apparent horizon location in each of the coordinate planes for the transformed Schwarzschild initial data. The numerical data are represented by solid lines, and the analytic data by symbols. The surface is pure $L=2$, although the finder was allowed to search through the $L=4$ coefficients as well. The computed coefficients are found to roughly 0.1% accuracy.
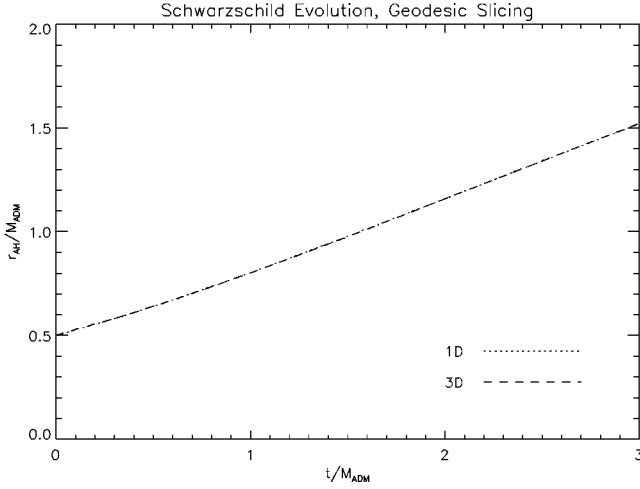
FIG. 7. The apparent horizon location for 1D and 3D Schwarzschild evolutions using geodesic slicing. The 1D data were obtained using 128 grid points and resolution $\Delta r = 0.0375M$, where M is the mass of the black hole. The 3D data were obtained using 64^3 grid points and resolution $\Delta x = 0.075M$. Only the $l = 0$ contribution to the 3D apparent horizon is plotted but the other terms in the $L = 4$ series are negligible, as discussed in the text.

spacetime evolution, which becomes inaccurate for $t > 20M$, although we note that the difference at the end of the run is still only about a grid zone.

In both the geodesic and maximal cases, the AH finder accounted for a large portion of the total CPU time. For the geodesic case the code ran 160 timesteps, invoking the finder once every $0.3M$ in time (11 times total). In this case, the finder constituted approximately 90% of the CPU time. For the maximal slicing case the code was run for 1100 timesteps, calling the finder every $2M$ (14 times total). In this case, 40% of the CPU time was spent in finding the
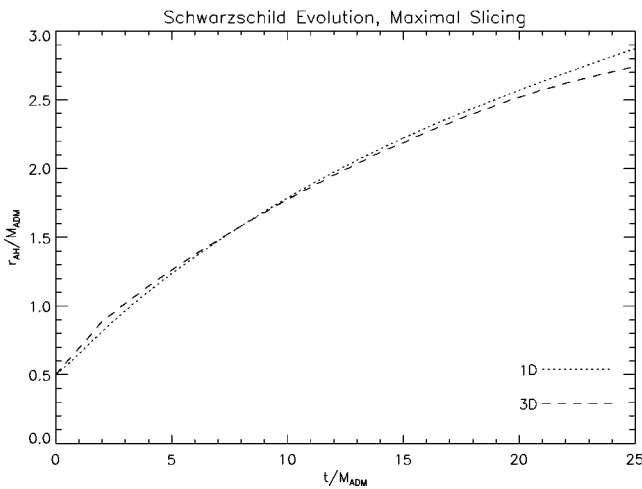

FIG. 8. The apparent horizon location for 1D and 3D Schwarzschild evolutions using maximal slicing. The 1D data were obtained using 130 grid points and resolution $\Delta r = 0.1M$, the 3D data using 130^3 grid zones and resolution $\Delta x = 0.1M$. We note that the agreement is within a grid zone even to the end of the calculation, when the 3D evolution becomes inaccurate.

horizon. The horizon finder with a $L = 4$ axisymmetric multipole expansion is thus approximately 50–100 times slower than a single update cycle in the hyperbolic evolution (although we note that when the elliptic maximal slicing equation is solved, the relative performance in the solver improves significantly). A factor of roughly 10 can be gained by reducing the expansion order to $L = 0$.

2. Misner 2BH collision

A more difficult evolution scenario is to capture the horizon surfaces as two black holes collide and merge. Our ''G'' code is used to evolve the two black hole Misner data set, described in Sec. III A 2, for a time sufficiently long that we can test the AH finder on this dynamic spacetime.

To evolve the initial data, we use a zero shift vector and an algebraic lapse of the form

$$\alpha = \alpha_o (1 + \log \hat{\gamma}), \qquad (26)$$

where $\hat{\gamma}$ is the conformal 3-metric determinant and α_o is the lapse on the initial time slice, which we take to be the Cadez [33] lapse

$$\alpha_o = \frac{1}{\psi} \left[1 + \sum_{n=1}^{\infty} (-1)^n \frac{1}{\sinh n\mu} \left(\frac{1}{+r_n} + \frac{1}{-r_n} \right) \right]. \quad (27)$$

The solution (27) solves the maximal equation in time symmetry with $\alpha = 0$ as a boundary condition on the throats. Algebraic lapses of the form (26) are singularity avoiding and produce evolutions similar to maximally sliced spacetimes [29].

The calculation is run on a 64^3 grid with $\Delta x = 0.1$ for a time of $t = 10M$ using an expansion to order $L = 4$. As our interest is in testing the ability of the solver to locate the AH before and after the surface merger event, it suffices to evolve a data set with a low value for the Misner parameter, which is computationally less expensive in evolution. Here we show results for the $\mu = 1.5$ case which has, as initial data, two coalesced black holes with a common event horizon, but two *distinct* trapped surfaces at the two throats. A common apparent horizon encircling both throats forms at time $t \sim 1.6M$.

Figure 9 plots the surfaces found at each time the finder is called ($t = 0$, 2.5, 5, 7.5 and $10M$, where M is the Arnowitt Deser-Misner (ADM) mass, and with the surfaces increasing in radius at the later times). At $t = 0$, the solver correctly finds the throat as the surface, centered off the origin. The finder can subsequently be prevented from locking onto the throat (which remains a trapped surface throughout the evolution) by restricting the range of radii over which the function $F(\theta, \phi, r)$ is evaluated, and by resetting the center of the surface. Unfortunately, there is no analytic result to compare against the computed location of the AH at the later times. Instead, we overlay the 3D computed AH surfaces with the results from our 2D axisymmetric code evolving the same initial data. The surfaces determined with these two different methods (3D minimization vs ODE integration) applied to the two different constructions of the spacetime (3D Cartesian evolution vs 2D axisymmetric evolution) basically agree
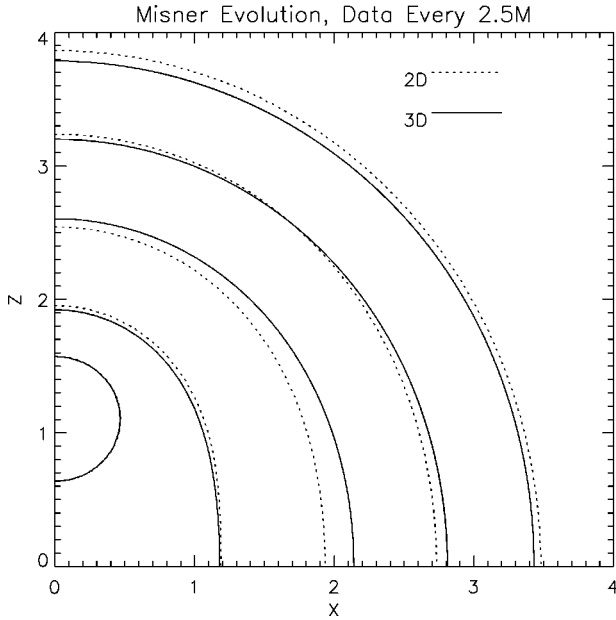
FIG. 9. Apparent horizon locations in the 3D evolution of the $\mu=1.5$ Misner two black hole data. The surfaces are plotted at times $t=0$, 2.5, 5, 7.5 and $10M$, where M is the ADM mass of the spacetime, and the surfaces increase in radius with time. The evolution is performed using a 64^3 grid with resolution $\Delta x=0.1$ and a multipole expansion of order $L=4$. Also shown are the corresponding horizons found in the 2D axisymmetric evolutions. The surfaces from the two calculations agree nicely, although we note that an exact correspondence is not expected due to different shift and lapse functions.

with one another. Nevertheless, we note that in the figure the two sets of surfaces are not exactly the same in coordinate space, as they should *not* be, since we are using different lapse and shift functions in the two cases. However, the shift vector is of magnitude $|\beta|\sim10^{-3}$ in the region of the AH, so we do not expect this effect to exceed the grid spacing scale over the time interval of the calculation. Also, the algebraic lapse used in the 3D code is typically larger than the maximal slicing lapse in the 2D code by a fractional difference $\Delta\alpha\sim0.02$ near the AH. This should also have a small effect on the coordinate position of the AH except at late times. In fact, the maximum differences in the AH location between the 2D and 3D calculations is only slightly more than a grid cell. The differences may also be attributed to inaccuracies in the evolution; as born out in computing the mass of the AH at different times. At $t=2.5M$, after a common surface forms to surround both throats, we find $M_{AH}=2.28$, compared to the 2D result of 2.36. However, by $t=10M$, the error in the mass of the computed surface increases to roughly 18% as the evolution becomes less accurate. These errors are attributable to numerical inaccuracies in the evolution and not the AH finder routine, in particular, they are unrelated to the multipole order used, since the surface becomes more spherical in time.

3. Black hole plus Brill wave

One final test of the solver in real time evolutions is a Schwarzschild black hole plus a Brill wave. The initial data
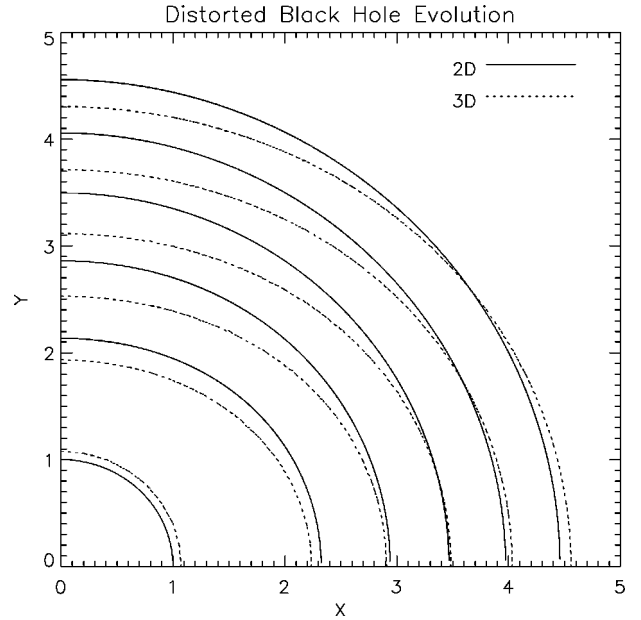

FIG. 10. Coordinate location of the AH found in the 2D and 3D evolutions of the Brill wave plus black hole spacetime. The surfaces are shown starting at $t=0$ with time intervals of $2m_0=1.12M$, where $M=3.54$ is the ADM mass of the spacetime. Although we do not expect identical results due to different kinematic conditions in the two cases, the surfaces differ at most by little more than two grid cells. The evolution is performed on a 66^3 grid with $\Delta x=0.2$.

is the same as that discussed in Sec. III A 3 with shape parameters $(\eta_0,\sigma,n)=(0,1,2)$, scale parameter $m_0=2$ and amplitude $a=-0.5$. For this set of parameters, the ADM mass of the spacetime is $M=1.77m_0=3.54$. The Hamiltonian constraint is solved for the conformal factor in our 2D axisymmetric code, then interpolated onto a 66^3 Cartesian grid with $\Delta x=0.2=0.056M$. The data is evolved with a timestep $\Delta t=0.25\Delta x=0.014M$, calling the horizon finder once every $m_0=0.56M$ intervals of time. The shift vector is set to zero and the lapse function is computed from the maximal slicing condition.

Figure 10 shows the horizon shapes and locations in the 3D calculation at various times with intervals of $2m_0=1.15M$, starting at $t=0$. The multipole order used in this calculation is $L=4$, with $m=0$ to reduce the computational time. The higher order expansion is needed here to describe the oblate shape of the horizons. For the most part, the solver required only about five iterations to converge when the previous solution is given as the initial guess to the finder. Also shown in Fig. 10 are the corresponding surfaces found in our 2D axisymmetric code. Once more we note that the slicing and shift conditions differ in the two cases, so we do not expect the surfaces to coincide precisely. However as the differences between the lapse functions and shift vectors are small ($|\beta|\sim10^{-3}$ and $\Delta\alpha\sim0.07$ in regions near the horizon except near the z-axis), the solutions do agree nicely. In and around the x-y plane, the solutions match to within half a grid cell. Greater differences, however, are found along the z-axis, where the two surfaces are displaced by a maximum of roughly two grid cells. This is attributed in part
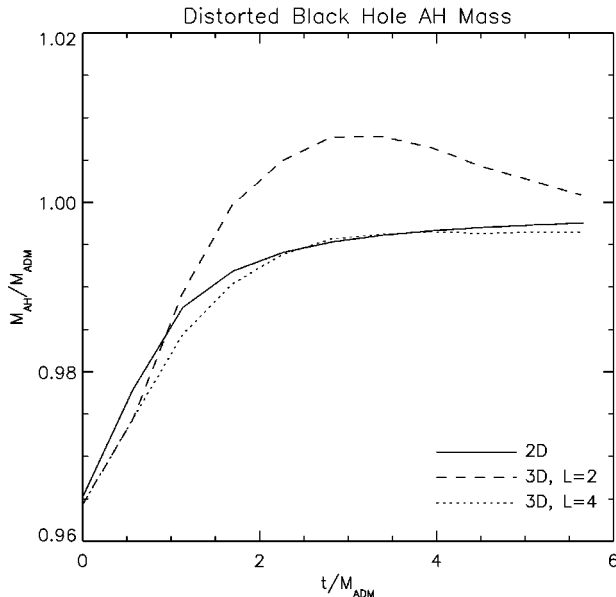
FIG. 11. Comparison of the apparent horizon masses computed from the 2D and 3D evolutions of the Brill wave plus black hole spacetime. The AH mass increases initially as the Brill wave falls into the black hole. By $t \sim 6M$, the mass approaches $0.997M$ and the 2D and $L=4$, 3D results differ by just 0.1% at this time. We also show the corresponding masses computed from the surfaces found with an $L=2$ multipole expansion. The low order expansion is clearly not adequate in resolving the surface at early times when the horizon is most distorted.

to a bigger $\Delta \alpha$ (~ 0.1) near the z-axis, which results from the imposed asymmetry in the lapse function due to the nearness of the outer boundaries, where we enforce the spherical Schwarzschild lapse as a boundary condition in the maximal equation used in the 2D simulation.

Again, a more geometrical comparison or test of the solver is the mass of the surface found. The horizon mass is defined as $M_{AH} = \sqrt{A_{AH}/16\pi}$, where A_{AH} is the area of the surface. Figure 11 plots the AH mass as a function of time for the 2D and the $L=4$, 3D evolutions. In both cases, the mass increases at first, as the gravitational waves fall into the black hole, reaching $M_{AH} \sim 0.997M$ at $t \sim 6M$. The masses in the two cases differ by only 0.1% at $t \sim 6M$. For comparison we also plot M_{AH} for the surface found using a lower order $L=2$ multipole expansion. At early times, when the horizon is most distorted, the $L=2$ expansion is clearly not adequate to resolve the horizon shape, as evidenced by the AH mass which exceeds the ADM mass by about 1%. How-

ever, as the black hole settles down into a quasi-static state, the surface becomes more spherical and the $L=2$ solution approaches both the 2D and the $L=4$, 3D results, differing from the 2D result by about 0.35% at $t \sim 6M$.

IV. CONCLUSIONS

We have developed a promising general 3D method of finding the AH in a numerically constructed spacetime based on a minimization procedure. In this paper we have applied the method and demonstrated that it works for spacetime data which are not time symmetric, and data sets which are obtained in actual numerical evolutions.

The major advantage of this method is that the minimization procedure is much better understood than the corresponding problem of solving the elliptic equation, and well-tested routines are available for solutions. The major drawback of the method is that, for AH surfaces which are not smooth, and which deviate significantly from sphericity in coordinate space, the higher dimensional minimization procedure can be computationally expensive. With our present implementation of the finder using Powell's routine, we are limited to searching for AH surfaces at every 50, or so, evolution cycles, instead of continually monitoring the AH throughout the numerical evolution, as would be our final goal. In future implementations of the method, we anticipate developing a more sophisticated minimization routine using derivative information to speed up the procedure, as well as other means to improve the robustness and efficiency of the code. Our code, which is optimized for both the C90 and massively parallel CM5 machines, together with documentation, will be made available on our servers http:// jean-luc.ncsa.uiuc.edu and http://wugrav.wustl.edu.

[1] A. A. Abramovici *et al.*, Science **256**, 325 (1992).
[2] S. Hughes *et al.*, Phys. Rev. D **49**, 4004 (1994).
[3] J. Libson *et al.*, Phys. Rev. D **53**, 4335 (1996).
[4] S. W. Hawking and G. F. R. Ellis, *The Large Scale Structure of Spacetime* (Cambridge University Press, Cambridge, England, 1973).
[5] P. Anninos *et al.*, Phys. Rev. D **50**, 3801 (1994).

[6] J. Thornburg, Ph.D. thesis, University of British Columbia, 1993.
[7] E. Seidel and W.-M. Suen, Phys. Rev. Lett. **69**, 1845 (1992).
[8] P. Anninos *et al.*, Phys. Rev. D **51**, 5562 (1995).
[9] A. Čadež, Ann. Phys. (N.Y.) **83**, 449 (1974).
[10] N. T. Bishop, Gen. Relativ. Gravit. **14**, 717 (1982).
[11] G. Cook and J. W. York, Phys. Rev. D **41**, 1077 (1990).

[12] K. P. Tod, Class. Quantum Grav. **8**, L115 (1991).

[13] D. Bernstein, Ph.D. thesis, University of Illinois Urbana-Champaign, 1993.

[14] T. Nakamura, Y. Kojima, and K. Oohara, Phys. Lett. **106A**, 235 (1984).

[15] A. J. Kemball and N. T. Bishop, Class. Quantum Grav. **8**, 1361 (1991).

[16] J. Thornburg, Phys. Rev. D **54**, 4899 (1996).

[17] M. F. Huq, S. A. Klasky, M. W. Choptuik, and R. A. Matzner (in preparation).

[18] J. Libson, J. Massó, E. Seidel, and W.-M. Suen, in *The Seventh Marcel Grossman Meeting: On Recent Developments in Theoretical and Experimental General Relativity, Gravitation, and Relativistic Field Theories*, edited by R. T. Jantzen, G. M. Keiser, and R. Ruffini (World Scientific, Singapore, 1996), p. 631.

[19] D. S. Brill and R. W. Lindquist, Phys. Rev. **131**, 471 (1963).

[20] K. Eppley, Phys. Rev. D **16**, 1609 (1977).

[21] T. W. Baumgarte *et al.*, Phys. Rev. D **54**, 4849 (1996).

[22] C. Gundlach, Phys. Rev. D **57**, 863 (1998).

[23] J. York, in *Frontiers in Numerical Relativity*, edited by C. Evans, L. Finn, and D. Hobill (Cambridge University Press, Cambridge, England, 1989), pp. 89–109.

[24] G. Gibbons, Commun. Math. Phys. **27**, 87 (1972).

[25] K. Thorne, Rev. Mod. Phys. **52**, 285 (1980).

[26] W. H. Press, B. P. Flannery, S. A. Teukolsky, and W. T. Vetterling, *Numerical Recipes* (Cambridge University Press, Cambridge, England, 1986).

[27] D. Bernstein *et al.*, Phys. Rev. D **50**, 5000 (1994).

[28] D. Bernstein, D. Hobill, E. Seidel, and L. Smarr, Phys. Rev. D **50**, 3760 (1994).

[29] P. Anninos *et al.*, Phys. Rev. D **52**, 2059 (1995).

[30] L. Smarr, A. Čadež, B. DeWitt, and K. Eppley, Phys. Rev. D **14**, 2443 (1976).

[31] P. Anninos *et al.*, Phys. Rev. D **52**, 2044 (1995).

[32] S. Brandt and E. Seidel, Phys. Rev. D **54**, 1403 (1996).

[33] A. Čadež, Ph.D. thesis, University of North Carolina at Chapel Hill, 1971.